Optically-Induced Symmetry Breaking via Nonlinear Phononics

Jared S. Ginsberg[1,#,*], M. Mehdi Jadidi[1,#], Jin Zhang[2,#,*], Cecilia Y. Chen[3], Sang Hoon Chae[4], Gauri N. Patwardhan[1,5], Lede Xian[2], Nicolas Tancogne-Dejean[2], Kenji Watanabe[6], Takashi Taniguchi[7], James Hone[4], Angel Rubio[2,8,*], and Alexander L. Gaeta[1,3,*]

[1]*Department of Applied Physics and Applied Mathematics, Columbia University, New York, New York 10027, USA*
[2]*Max Planck Institute for Structure and Dynamics of Matter and Center for Free-Electron Laser Science, Hamburg 22761 Germany*
[3]*Department of Electrical Engineering, Columbia University, New York, New York 10027, USA*
[4]*Department of Mechanical Engineering, Columbia University, New York, New York 10027, USA*
[5]*School of Applied and Engineering Physics, Cornell University, Ithaca, New York 14853, USA*
[6] *Research Center for Functional Materials, National Institute for Materials Science, 1-1 Namiki, Tsukuba 305-0044, Japan*
[7] *International Center for Materials Nanoarchitectonics, National Institute for Materials Science, 1-1 Namiki, Tsukuba 305-0044, Japan*
[8]*Center for Computational Quantum Physics, Simons Foundation Flatiron Institute, New York, NY 10010 USA.*

[#]These authors contributed equally to this work
* *jsg2208@columbia.edu (J.S.G.), jin.zhang@mpsd.mpg.de (J.Z.), angel.rubio@mpsd.mpg.de (A.R.), and alg2207@columbia.edu (A.L.G.)*

Abstract: Optical nonlinearities in solids reveal information about both the in-plane rotational and out-of-plane inversion symmetries of a crystal. In the van der Waals material hexagonal boron nitride (hBN) both these symmetries and the linear vibrational properties have led to the rich physics of mid-infrared phonon-polaritons. However, the role of strong electron-phonon nonlinearities requires further study. In this work, we investigate both theoretically and experimentally the rich interplay of phonon anharmonicity and symmetry in phonon-polariton mediated nonlinear optics. We show that large enhancements ($>30\times$) of third-harmonic generation occur for incident femtosecond pulses that are resonant with the hBN transverse optical phonons. In addition, we predict and observe large transient sub-picosecond duration second-harmonic signals during resonant excitation, which in equilibrium is forbidden by symmetry. This surprising result indicates that instantaneous crystal inversion symmetry breaking can be optically induced and controlled via phonon interactions by both the power and polarization of the pump laser.

Introduction

The generation of optical harmonics in solids provides a window into the optical susceptibility, band-structure, and underlying symmetries of crystals, each of which can dramatically affect the nonlinear frequency-conversion process [1–3]. Symmetries, more so than any other factor, dictate the allowed higher-order processes in a given nonlinear system [4]. These properties become frequency independent far from any resonances, as is the case in the visible and near-infrared regime where many high-order harmonic generation measurements take place [5]. However, in the mid-infrared regime, polar crystals support lattice collective oscillations that can be resonantly driven by an optical field. At frequencies near these phonon resonances the linear optical response of the crystal is significantly modified, manifesting for example as a peak in the real permittivity [6]. Under increased resonant excitation using femtosecond laser pulses, the amplitude of the ionic motion can become nonlinear with the incident field strength. For bulk materials such as $LiNbO_3$ and $GaAs$, phonon-induced enhancements of optical nonlinearities [7–10] occur in this regime. Furthermore, these ionic modes can alter the symmetry properties of the crystal, leading to transient nonlinear optical effects such as those observed in $SrTiO_3$, which can be driven into a metastable non-centrosymmetric state following prolonged exposure to a phonon-resonant pump [11].

A strong phonon resonance in the mid-IR is present in the van der Waals crystal hexagonal boron nitride (hBN), with a transverse optical (TO) phonon mode at 7.3 µm free-space wavelength (170 meV) [12]. The relatively light constituent atoms of hBN make this one of the most energetic TO phonons, accessible by ultrafast table-top lasers. hBN has an energetically favorable AA' stacked lattice in equilibrium, with alternating boron and nitrogen atoms sitting one on top of the other. An illustration of the resonantly driven, in-plane displacement of atoms for the TO (E_{1u}) mode of hBN [13] is presented in Fig. 1a. At the point where the photon and phonon dispersion curves meet, an anti-crossing emerges in the hBN band structure, and the crystal hosts new hybrid modes called phonon-polaritons [14]. These have been the subject of intense study due to their long-range propagation [15].

The natural hyperbolicity of the hBN TO phonon also makes it an attractive platform for tight confinement of optical energy, and therefore for enhancing nonlinearities and light-matter interactions within relatively large volumes [6]. We will extend the scope of these light-matter processes by showing that it is possible to further enhance optical nonlinearities by exploiting the
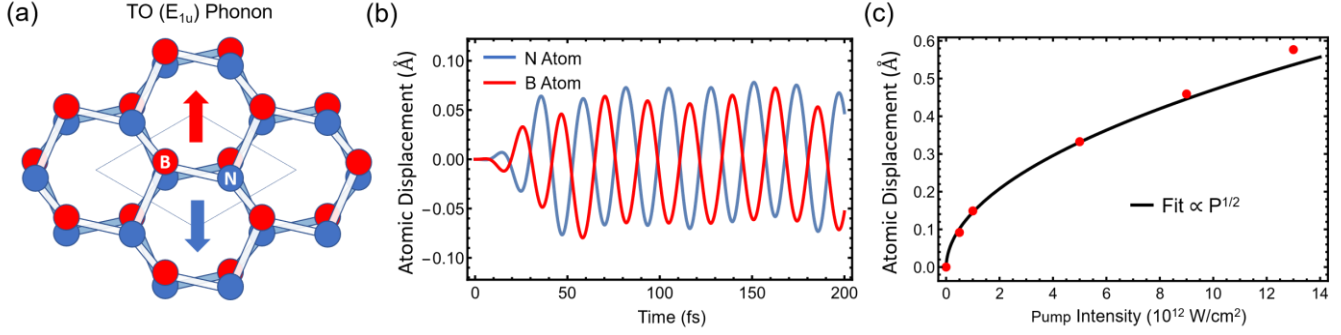
Figure 1: (a) Honeycomb lattice arrangement of hexagonal boron nitride. Arrows illustrate the motion of atoms under resonant optical excitation. The two species move oppositely from each other in plane and across all layers for the IR-active TO (E_{1u}) mode, but same species atoms move oppositely in adjacent layers for TO (E_{2g}). (b) Simulated atomic displacements of boron and nitrogen ions in TO (E_{1u}) excited hBN. A 25-fs FWHM, 1 x 10^{12} W/cm^2 pulse excites the lattice dynamics. The TDDFT simulations do not include any damping terms through which to estimate the relaxation time. (c) Peak amplitude of atomic displacements as a function of pump intensity, fit to $I^{1/2}$ with a small linear-in-intensity correction. Displacements nearing 5% of the equilibrium lattice constant are achievable before the onset of damage.

strong hyperbolic confinement for even greater electron-phonon coupling. Specifically, in this work we show enhanced emission from the phonon-electron contributions to optical harmonic generation in hBN. We theoretically predict and demonstrate experimentally the nonlinear response of thin hBN crystals associated with this TO phonon mode at 7.3 µm. By sweeping a significant bandwidth of the mid-IR we demonstrate a greatly enhanced on-resonance phononic contribution to third-harmonic generation (THG) when hBN is pumped at its TO phonon-polariton. In addition, through time-resolved measurements, we confirm that when TO phonons of hBN are strongly excited, the inversion symmetry of the crystal is broken instantaneously and transient second-harmonic generation (SHG) occurs, which is forbidden in the bulk at equilibrium (with few exceptions) [16–18]. The SHG yields are studied as a function of the power and polarization of both the phonon-inducing pump and harmonic-generating probe, from which preferential symmetry axes for SHG are identified.

Results

Phonon-enhanced third-harmonic generation: We first characterize theoretically the ionic displacements in bulk hBN under resonant excitation with 25-fs FWHM pulses by performing time dependent density-functional theory (TDDFT) simulated atomic oscillations panning 200-fs, or roughly 8 times the theoretical pulse duration (see Fig. 1b). For a modest input intensity of 7 x 10^{10} W/cm^2, we estimate that the phonon amplitude is 1% of the equilibrium lattice constant. While the period of the lattice oscillation is 25-fs, which is consistent with the expected phonon frequency, the relaxation time cannot be theoretically determined due to a lack of dissipative pathways. The amplitudes of atomic motion are plotted as a function of pump intensity in Fig. 1c. The displacements predicted by TDDFT calculations are fit by $I^{1/2}$ with deviations appearing at large intensities and reach nearly 5% of the equilibrium lattice constant (2.5 Å) [19] at 10 TW/cm^2. The time-dependent electronic current is extracted, and from this we generate the theoretical harmonic spectra employed throughout this work (see Methods). This process is repeated for wavelengths below, at, and above 7.3 µm, and the integrated theoretical THG yields are plotted in Fig. 3a as green dots.

We show the integrated and normalized experimental (Fig. 2a) THG amplitudes for a range of pump wavelengths from 3 µm to 9.5 µm in Fig. 3a as blue dots, which are in excellent agreement with the calculations discussed in Fig. 1 and plotted as green dots in Fig.3a. The third-harmonic exhibits a strong peak for pump wavelengths near the TO phonon resonance at $\lambda = 7.3$ µm. As this wavelength is far from any electronic or excitonic resonances, the enhancement must be phononic in nature. We fit the data to a Lorentzian and extract a resonance full-width at half-maximum of 500 nm. THG yields are below the noise level for all λ_{pump} less than 6 µm or greater than 9 µm, compared to that of the resonant signal which yields at least a 30-fold increase, and thus the phononic enhancement of the THG coefficient at the phonon-polariton wavelength is significantly greater than the purely-electronic component in this regime. In Fig. 3b we plot the measured intensity dependence of the THG signal for $\lambda_{pump} = 7.3$ µm. The fit to a cubic function indicates that the measured nonlinearity is third-order and that the scaling is perturbative, even at high intensities [20]. We note that a similar effect has been observed in the phononic second-harmonic generation of LiNbO$_3$, which also remained in the perturbative regime at higher-than-expected intensities. Also, we propose that subwavelength structures that support confined phonon-polaritons [6,21] can drastically enhance the phonon-induced nonlinearity in the same way that they dramatically enhance electronic nonlinearities.
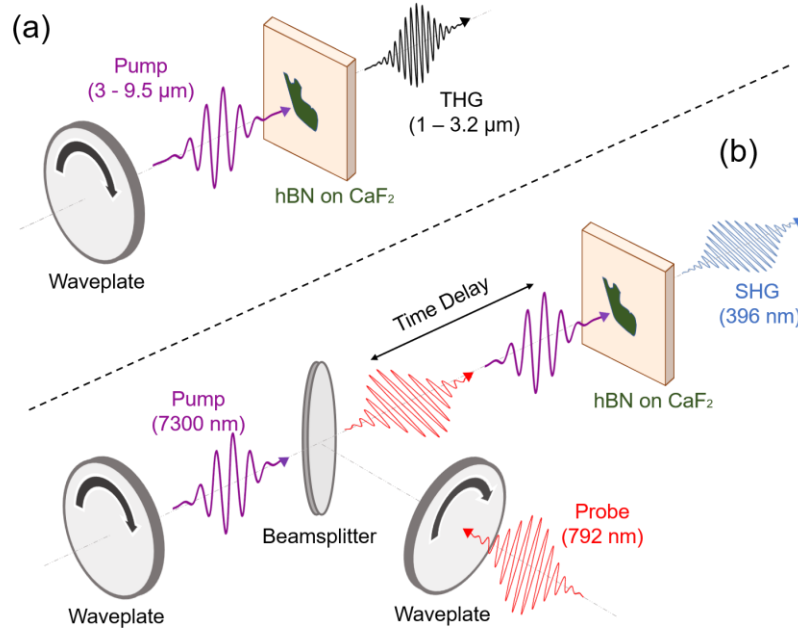
Figure 2: (a) Experimental setup for THG experiments. Detection is performed with PbS and MCT detectors, a lock-in amplifier, and boxcar-averaging. (b) Experimental setup for pump-probe SHG experiments. The time-delay is controlled by a mechanical delay stage with sub-1 µm step size. The pump and probe are both focused onto the sample with a reflective objective with 0.5 numerical aperture. Detection is performed with a silicon photomultiplier tube and lock-in amplifier.

We also performed TDDFT simulations of the wavelength dependence of a higher-order harmonic (HHG) spectra of bulk hBN See supplementary Fig. S1 for two different pump lasers with a wavelength of $\lambda_{pump} = 7.3$ µm (polarized parallel to the TO mode) and $\lambda_{pump} = 6.2$ µm (polarized parallel to the LO mode). Changing the wavelength and polarization of the pump laser can lead to the excitation of different phonon modes and lead to significant modulation of the HHG spectra. Excitation of either the TO or LO mode leads to noticeable modifications of the high-harmonic spectra, with the TO (E_{1u}) enhancement being one order of magnitude greater than that caused by LO excitation. Furthermore, more intense laser pulses can introduce larger atomic displacements and lead to larger nonlinearity. As seen from a pump intensity of $2.5 \times 10^{10}\,\mathrm{W/cm^2}$, the high-harmonic yields can be increased in a wide energy regime, and the high harmonic generation plateau is enhanced (Fig. S2), which is attributed to the increased atomic movement and enhanced nonlinearity.

Phonon-induced transient second-harmonic generation: Multilayer hBN has inversion (and 6-fold rotational) symmetry due to the natural 2H stacking of its van der Waals structure [22]. Any contribution to SHG in few- to many- layer hBN is therefore restricted only to the broken inversion symmetry cases of interfaces and an odd number of layers and is inherently weak [16]. By conducting ultrafast pump-probe experiments we show that the crystal inversion symmetry can instead be controllably broken by excitation of the IR-active TO (E_{1u}) phonon, which leads to a finite second-order susceptibility. For large amplitudes of the laser-driven lattice deformation, our simulations reveal the emergence of an ultrafast, transient SHG signal from a secondary 800 nm laser pulse, as shown in Fig. 4a. We distinguish this induced SHG from any nearby odd-order processes by performing the calculations in the following two different ways: i) with a 7.3 µm pump field, and ii) using the time-evolution of an equivalently distorted lattice and no resonant photons. In both cases the signal at harmonic order 2 emerges, confirming the principal role of the broken symmetry. Furthermore, simulations confirm that in the case of the Raman-active hBN TO (E_{2g}) phonon which preserves inversion symmetry, even-order nonlinearity cannot be observed.

The experimentally measured SHG signal at 396 nm is presented in Fig. 4b as a function of the time delay between 792 nm and 7.3 µm pulses. The probe pulse from an amplified Titanium-Sapphire laser and the pump pulse from a mid-infrared OPA and difference frequency generation module are scanned in time by a mechanical delay line. The powers and relative polarizations are set with filters and half wave plates (HWP), and the two beams are then combined on a beamsplitter before being focused onto the sample by a reflective objective (the experimental setup is shown in Fig. 2b, with further details in Methods). When the probe pulse precedes the pump pulse, no SHG is measured, indicating that the interface SHG and odd layer-number contributions
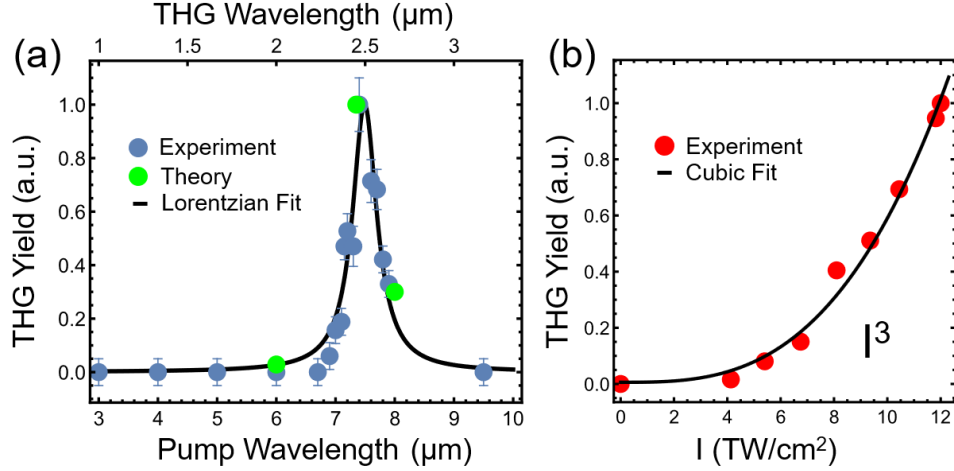
Figure 3: (a) Normalized third-harmonic generation yields of 120-fs pulses as a function of pump wavelengths throughout the mid-IR. THG yields are below the noise level for all wavelengths less than 6 μm or greater than 9 μm. Within a roughly 1 μm bandwidth of the phonon-polariton resonance, a THG enhancement of 30x is observed. The black line is a Lorentzian fit to the data (blue dots) with full-width at half-maximum of 500 nm. The green dots were obtained by integrating the third-harmonic signal in TDDFT simulations and show excellent agreement with experiments. (b) Normalized intensity dependence of THG pumped on-resonance at 7.3 μm and measured at 2.43 μm. The data is a close fit to I^3, indicating that the nonlinear process is scaling perturbatively.

are below the noise floor. The time-resolved SHG then displays a finite signal at the zero-time delay, when the probe pulse's arrival coincides with the strong excitation of the hBN phonon-polariton. The SHG signal relaxes back to zero with a time constant of approximately 120 fs, which is approximately twice the pump pulse duration. When pumped far off-resonance, no SHG is measured. In Fig. 4c and 4d we show the dependence of the SHG yield on the intensity of the probe and pump, respectively. A quadratic dependence of the SHG intensity on the probe power is observed, as expected for a second-order nonlinear process. The linear scaling of the SHG signal with respect to the mid-IR intensity in Fig. 4d implies a direct dependence of the transient SHG process on the ionic displacements. These dependences match those reported for $SrTiO_3$, in which an SHG yield in low temperature experiments was found to steadily increase over hours of total pump exposure and persist for hours after, with ps-scale modulations that also increase in frequency with total exposure time [11]. Another similar effect with a very long response time was observed in the naturally inversion-symmetry-broken van der Waals material WTe_2 [23]. However, in this case the effect of a shear strain and lattice displacement was to eliminate the naturally present SHG, which is the opposite of our observed effect.

Next, we establish the dependence of the ultrafast SHG on the orientation of the pump and probe polarizations with respect to the crystal high-symmetry axes. Figure 5a gives the total normalized SHG yield for 360° rotation of both pulses (180° rotation is measured and the data is then mirrored). We observe a polarization behavior unique from either the inherent 6-fold $\chi^{(2)}$ or isotropic $\chi^{(3)}$ symmetries of purely electronic hBN nonlinearities [24]. Specifically, the emission closely follows the functional form,

$$SHG(\theta, \phi) = [\, \alpha \, Cos(3\theta)^2 + \beta \, Sin(3\theta)^2 \,] \, Cos(\theta - \phi)^2, \tag{1}$$

where θ and ϕ are the angles of the pump and probe relative to the zigzag (ZZ) axis of the crystal, respectively, and α and β determine the relative strengths of the emission along the ZZ and Armchair (AC) axes, respectively. SHG yields peak only along ZZ axes that are being resonantly driven with a phonon-polariton. This is most clearly visible in the linecuts of the probe polarization dependence for pump fields aligned parallel to the AC and ZZ axes, given in Fig. 5b. Even when the pump excitation is aligned with an AC axis, the two adjacent ZZ oriented $TO(E_{1u})$ phonons break the inversion symmetry, and we observe SHG, whereas the ZZ axis at exactly 90° from that excitation shows no emission. From Fig. 5 we determine that the phonon-mediated SHG is at least 3 times greater parallel to ZZ than AC directions. This is supported by time-dependent density functional theory (TDDFT) simulations in Fig. 5c, which identifies even-order nonlinearity along both symmetry axes, though much greater for the $TO(E_{1u})$ phonon than the relative π phase $LO(E_{1u})$.

Discussion

We have extended the light-matter interactions confined by the hyperbolic nature of the hBN phonon dispersion to a strongly
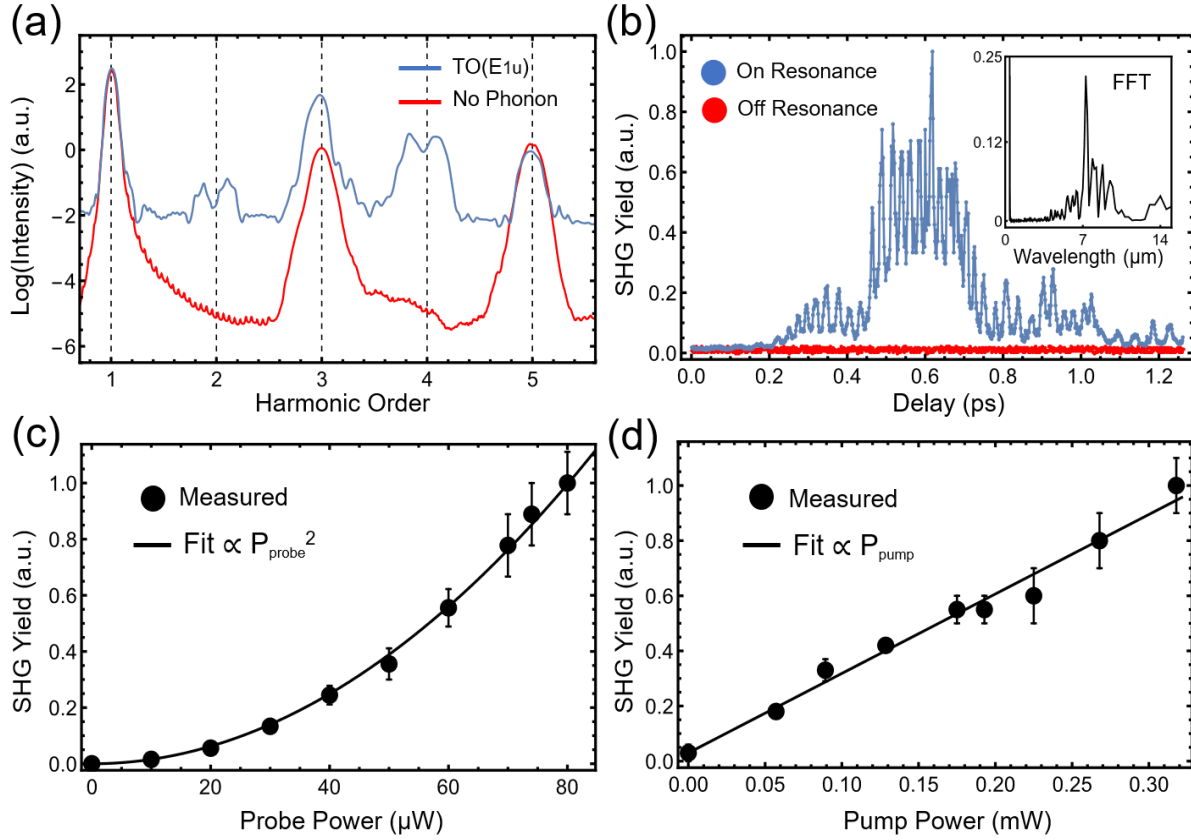
Figure 4: (a) TDDFT simulations show the emergence of even-order nonlinearity during resonant excitation of the TO phonon mode. (b) Time-resolved SHG yield (normalized) of the 792 nm probe pulse. While the pumps are temporally overlapped, an ultrafast second-order nonlinearity is measured. The inversion symmetry is restored following a 200-fs time constant, or about twice the pulse duration. The appearance of wings in the time-delay scan is a result of a non-perfectly Gaussian pulse, a result of strong atmospheric absorption. Inset: Fourier-Transform of the SHG time-delay. (c) Dependence of measured SHG yield on probe power. (d) Dependence of measured SHG on pump power. The SHG yield increases linearly with the phonon driving intensity.

nonlinear regime by demonstrating that the large electron-phonon coupling leads to a nearly two order of magnitude enhancement of SHG and THG. Efficient coupling of light to hBN phonon-polaritons at normal incidence places stringent requirements on the allowed optical excitation wavelength. For the free-space wavevector $\mathbf{k} = 0$, the required photon wavelength of 7.3 µm is fixed, independent of flake thickness [12]. With the energy-momentum conditions met, we have shown that efficient coupling of optical energy into the hBN lattice leads to anharmonic driving of the atoms. Phonon amplitudes can reach a few percent of the equilibrium lattice constant long before the onset of laser-induced damage according to TDDFT simulations. The anharmonicity of the ionic motion leads to a novel, enhanced nonlinearity, for which hBN is the most attractive platform in the mid-IR due to its relatively light constituent atoms. Saturation of the THG yield below its perturbative cubic scaling was not observed and is more likely to occur closer to the onset of sample damage. The extension of nonlinear phonon enhancement to higher-order nonlinearities and to two-color high-harmonic generation techniques will likely advance our understanding of electron-phonon coupling and nonlinearly-driven lattices.

Our results also establish SHG as a sensitive probe for ultrafast symmetry monitoring and eventually control, complementing earlier demonstrations on broken-inversion-symmetric transition metal dichalcogenides, while reducing the relaxation time scale by more than two orders of magnitude [23]. The presence of fast oscillations in the measured SHG on top of another transient but finite signal is indicative of a combination of effects. Whereas the fast fs-timescale oscillations appear to be coherent with the excited phonons, the constant pedestal suggests a second, rectified signal. This can occur, for example, when the coupling of the IR-active phonon to a Raman-active mode creates a new equilibrium position of the lattice atoms [11]. The maximum achievable yield is highly sensitive to the underlying symmetries of the hexagonal lattice, peaking along the ZZ axes where the greatest atomic displacements are known to occur. We note that the observed transient broken-inversion symmetry and atomic displacement can also be interpreted as a strong photo-induced strain field when the phonon mode is resonantly excited [25]. The
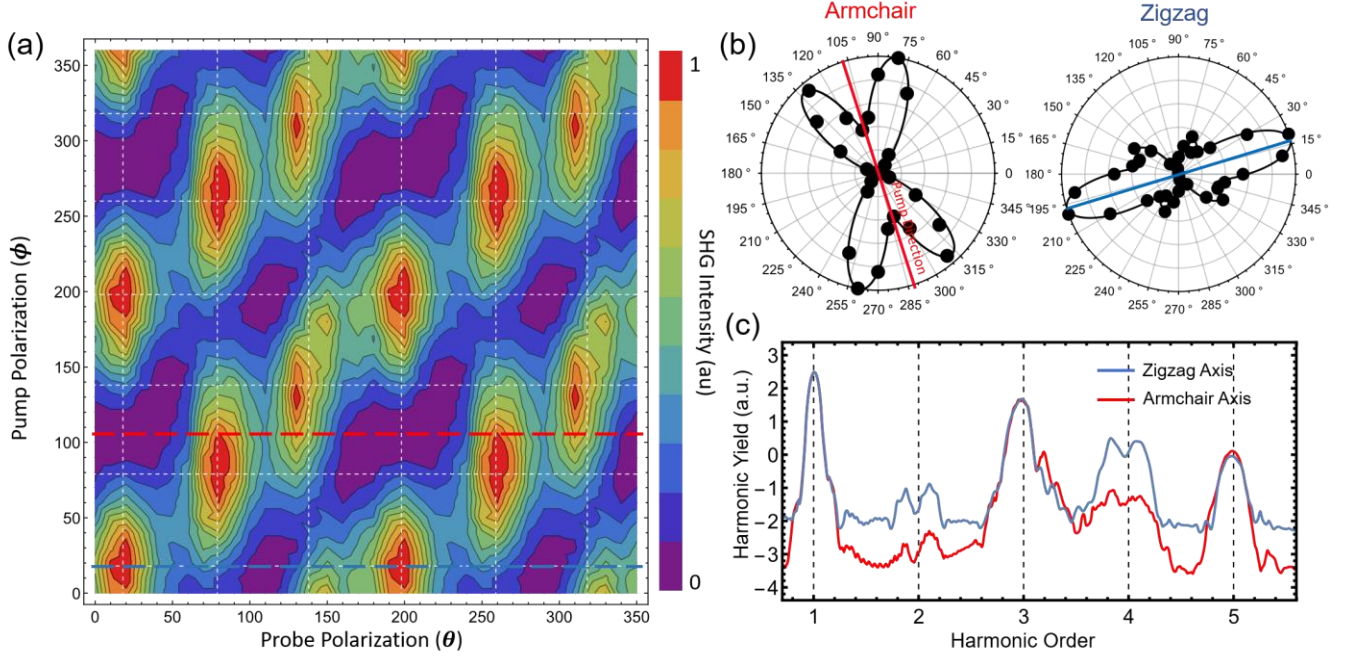
Figure 5: (a) Pump and probe polarization dependence of total SHG emission (normalized). White dashed lines indicate ZZ axes and are included as a guide for the eye and to emphasize the 60° periodicity. (b) Linecuts along the ZZ and AC axes from (a). Solid black lines are fit from Equation 1, with α and β as fit parameters. (c) TDDFT computed high-harmonic generation spectra for pump and probe pulses co-polarized along the ZZ (blue) and AC (red) directions. The TO(E_{1u}) phonon present along the ZZ axes leads to the greatest even order nonlinearity.

promise of optically-controllable strain in hBN lends itself to numerous other applications, from the tuning of photoluminescence [26] to optical control of van der Waals heterostructures, for which hBN is a common encapsulating material.

Methods

Theory: in the TDDFT simulations, the time evolution of the wave functions and the evaluation of the time-dependent electronic current were computed by propagating the Kohn-Sham equations in real space and real time, as implemented in the Octopus code [27,28], in the adiabatic LDA [29] (the findings and trends discussed in the present work are robust with different functionals) and with semi-periodic boundary conditions [28]. All calculations were performed using fully relativistic Hartwigsen, Goedecker, and Hutter (HGH) pseudopotentials [30]. The real-space cell was sampled with a grid spacing of 0.4 bohr and the Brillouin zone was sampled with a $42 \times 42 \times 21$ k-point grid, which yielded highly converged results. The boron nitride bond length is taken here as the experimental value of 1.445 Å. The laser was treated in the dipole approximation using the velocity gauge (that implies that we impose the induced vector field to be time dependent but homogeneous in space), and we used a sin-square pulse envelope. In all of our calculations, we used a carrier-envelope phase of f = 0 [31]. The full harmonic spectrum is computed directly from the total electronic current $\mathbf{j}(\mathbf{r}, t)$ as

$$HHG(\omega) = \left| FT\left(\frac{\partial}{\partial t} \int d^3\mathbf{r} \, \mathbf{j}(\mathbf{r}, t)\right) \right|^2, \qquad (2)$$

where FT denotes the Fourier transform. The atomic vibrations of phonon modes are prepared with the following two methods: (i) the time-evolution from a distorted atomic configuration along the phonon modes of 1% of the bulk hBN lattice. (ii) application of pump laser pulses with the same frequencies and polarizations of phonon modes. Our calculations confirm the two methods are equivalent in the simulations of high-harmonic generation.

Experiments: we performed the nonlinear experiments on high-quality hBN flakes with thicknesses of 10 to 50 nm and typical sizes of tens of microns. The flakes are exfoliated onto a CaF$_2$ substrate, chosen for its high transparency in both the visible and mid-infrared and its relatively small nonlinearity. For our long-wave infrared pump pulses we utilize an optical parametric

amplifier (OPA, Light Conversion HE Topas Prime) pumped by an amplified Titanium-sapphire laser system (Coherent Legend Elite) operating at a 1-kHz repetition rate with 6 mJ of pulse energy. The OPA produces 60-fs duration signal and idler pulses with center wavelengths in the near-IR. The parametric amplifier output is then used to seed an additional difference frequency generation (DFG) module for all mid-infrared measurements from λ_{pump} = 3 to 10 μm with pulse durations ranging from 70- to 120-fs. Pulse intensities are consistently set below the hBN damage threshold, which we estimate to be 50 TW/cm^2. For THG experiments the pump is focused onto an hBN flake using a 2-cm focal length CaF$_2$ lens, and the emitted THG signal is collected in a transmission geometry by an identical lens. After the residual pump beam is rejected by a short-pass filter, the remaining THG is measured on a PbS detector for harmonic wavelengths λ_{THG} below 1.7 μm, and on a liquid nitrogen-cooled MCT detector for all λ_{THG} greater than 2 μm.

For SHG measurements we modify the experimental setup to a pump-probe scheme with the addition of a 792 nm, 45-fs pulse from the same amplified Ti-Sapphire laser. A variable time-delay separates the 7.3 μm pump pulse that we use to excite the phonon, from the near-IR probe which produces the SHG signal at 396 nm. The intensity of both pulses is maintained at or below the (TW/cm^2) range, which is below the hBN damage threshold. The time delay between pulses is controlled by a mechanical delay line with sub-1-μm step size. The polarization of the pump and probe beams are independently rotated with zero-order half-wave plates and wire-grid polarizers before the pulses are combined on a beamsplitter. The collinear pump and probe are focused onto an hBN flake using a reflective objective (NA = 0.5), which ensures the same focal plane for the two beams with very different wavelengths. The SHG signal produced by the 792 nm pulse can be collected either in the reflection geometry by the reflective objective, or in transmission by a CaF$_2$ lens. The signal is then directed through a bandpass filter with a 10-nm bandwidth to reject the residual 792 nm and 7.3 μm light, as well as any unwanted $\chi^{(3)}$ signals, before detection on a fast photomultiplier tube (PMT) and lock-in amplifier.

Acknowledgements

References

1. R. Boyd, *Nonlinear Optics*, 3rd ed. (Elsevier, 2008).
2. A. A. Lanin, E. A. Stepanov, A. B. Fedotov, and A. M. Zheltikov, "Mapping the electron band structure by intraband high-harmonic generation in solids," Optica **4**, 516 (2017).
3. N. Klemke, N. Tancogne-Dejean, G. M. Rossi, Y. Yang, F. Scheiba, R. E. Mainz, G. Di Sciacca, A. Rubio, F. X. Kärtner, and O. D. Mücke, "Polarization-state-resolved high-harmonic spectroscopy of solids," Nature Communications **10**, 1319 (2019).
4. O. Neufeld, D. Podolsky, and O. Cohen, "Floquet group theory and its application to selection rules in harmonic generation," Nat Commun **10**, 405 (2019).
5. S. Ghimire and D. A. Reis, "High-harmonic generation from solids," Nature Physics **15**, 10–16 (2019).
6. J. D. Caldwell, A. V. Kretinin, Y. Chen, V. Giannini, M. M. Fogler, Y. Francescato, C. T. Ellis, J. G. Tischler, C. R. Woods, A. J. Giles, M. Hong, K. Watanabe, T. Taniguchi, S. A. Maier, and K. S. Novoselov, "Sub-diffractional volume-confined polaritons in the natural hyperbolic material hexagonal boron nitride," Nat Commun **5**, 5221 (2014).
7. A. von Hoegen, R. Mankowsky, M. Fechner, M. Först, and A. Cavalleri, "Probing the interatomic potential of solids with strong-field nonlinear phononics," Nature **555**, 79–82 (2018).
8. M. Först, C. Manzoni, S. Kaiser, Y. Tomioka, Y. Tokura, R. Merlin, and A. Cavalleri, "Nonlinear phononics as an ultrafast route to lattice control," Nature Phys **7**, 854–856 (2011).
9. A. Subedi, A. Cavalleri, and A. Georges, "Theory of nonlinear phononics for coherent light control of solids," Phys. Rev. B **89**, 220301 (2014).

10. T. Dekorsy, V. A. Yakovlev, W. Seidel, M. Helm, and F. Keilmann, "Infrared-Phonon–Polariton Resonance of the Nonlinear Susceptibility in GaAs," Physical Review Letters **90**, 4 (2003).

11. T. F. Nova, A. S. Disa, M. Fechner, and A. Cavalleri, "Metastable ferroelectricity in optically strained SrTiO$_3$," Science **364**, 1075–1079 (2019).

12. S. Dai, Z. Fei, Q. Ma, A. S. Rodin, M. Wagner, A. S. McLeod, M. K. Liu, W. Gannett, W. Regan, K. Watanabe, T. Taniguchi, M. Thiemens, G. Dominguez, A. H. C. Neto, A. Zettl, F. Keilmann, P. Jarillo-Herrero, M. M. Fogler, and D. N. Basov, "Tunable Phonon Polaritons in Atomically Thin van der Waals Crystals of Boron Nitride," Science **343**, 1125–1129 (2014).

13. R. Geick, C. H. Perry, and G. Rupprecht, "Normal Modes in Hexagonal Boron Nitride," Phys. Rev. **146**, 543–547 (1966).

14. S. Foteinopoulou, G. C. R. Devarapu, G. S. Subramania, S. Krishna, and D. Wasserman, "Phonon-polaritonics: enabling powerful capabilities for infrared photonics," Nanophotonics **8**, 2129–2175 (2019).

15. D. N. Basov, M. M. Fogler, and F. J. G. de Abajo, "Polaritons in van der Waals materials," Science **354**, (2016).

16. Y. Li, Y. Rao, K. F. Mak, Y. You, S. Wang, C. R. Dean, and T. F. Heinz, "Probing Symmetry Properties of Few-Layer MoS2 and h-BN by Optical Second-Harmonic Generation," Nano Lett. **13**, 3329–3333 (2013).

17. S. Kim, J. E. Fröch, A. Gardner, C. Li, I. Aharonovich, and A. S. Solntsev, "Second-harmonic generation in multilayer hexagonal boron nitride flakes," Opt. Lett., OL **44**, 5792–5795 (2019).

18. K. Yao, N. R. Finney, J. Zhang, S. L. Moore, L. Xian, N. Tancogne-Dejean, F. Liu, J. Ardelean, X. Xu, D. Halbertal, K. Watanabe, T. Taniguchi, H. Ochoa, A. Asenjo-Garcia, X. Zhu, D. N. Basov, A. Rubio, C. R. Dean, J. Hone, and P. J. Schuck, "Enhanced tunable second harmonic generation from twistable interfaces and vertical superlattices in boron nitride homostructures," Sci. Adv. **7**, eabe8691 (2021).

19. W. Paszkowicz, J. B. Pelka, M. Knapp, T. Szyszko, and S. Podsiadlo, "Lattice parameters and anisotropic thermal expansion of hexagonal boron nitride in the 10–297.5 K temperature range," Appl Phys A **75**, 431–435 (2002).

20. A. Spott, A. Becker, and A. Jaroń-Becker, "Transition from perturbative to nonperturbative interaction in low-order-harmonic generation," Phys. Rev. A **91**, 023402 (2015).

21. M. Tamagnone, A. Ambrosio, K. Chaudhary, L. A. Jauregui, P. Kim, W. L. Wilson, and F. Capasso, "Ultra-confined mid-infrared resonant phonon polaritons in van der Waals nanostructures," Science Advances **4**, eaat7189 (2018).

22. S. M. Gilbert, T. Pham, M. Dogan, S. Oh, B. Shevitski, G. Schumm, S. Liu, P. Ercius, S. Aloni, M. L. Cohen, and A. Zettl, "Alternative stacking sequences in hexagonal boron nitride," 2D Mater. **6**, 021006 (2019).

23. E. J. Sie, C. M. Nyby, C. D. Pemmaraju, S. J. Park, X. Shen, J. Yang, M. C. Hoffmann, B. K. Ofori-Okai, R. Li, A. H. Reid, S. Weathersby, E. Mannebach, N. Finney, D. Rhodes, D. Chenet, A. Antony, L. Balicas, J. Hone, T. P. Devereaux, T. F. Heinz, X. Wang, and A. M. Lindenberg, "An ultrafast symmetry switch in a Weyl semimetal," Nature **565**, 61–66 (2019).

24. A. A. Popkova, I. M. Antropov, J. E. Fröch, S. Kim, I. Aharonovich, V. O. Bessonov, A. S. Solntsev, and A. A. Fedyanin, "Optical Third-Harmonic Generation in Hexagonal Boron Nitride Thin Films," ACS Photonics **8**, 824–831 (2021).

25. S. H. Rhim, Y. S. Kim, and A. J. Freeman, "Strain-induced giant second-harmonic generation in monolayered 2H-MoX2 (X = S, Se, Te)," Appl. Phys. Lett. **107**, 241908 (2015).

26. N. Mendelson, M. Doherty, M. Toth, I. Aharonovich, and T. T. Tran, "Strain-Induced Modification of the Optical Characteristics of Quantum Emitters in Hexagonal Boron Nitride," Advanced Materials **32**, 1908316 (2020).

27. X. Andrade, D. Strubbe, U. D. Giovannini, A. H. Larsen, M. J. T. Oliveira, J. Alberdi-Rodriguez, A. Varas, I. Theophilou, N. Helbig, M. J. Verstraete, L. Stella, F. Nogueira, A. Aspuru-Guzik, A. Castro, M. A. L. Marques, and A. Rubio, "Real-space grids and the Octopus code as tools for the development of new simulation approaches for electronic systems," Phys. Chem. Chem. Phys. **17**, 31371–31396 (2015).

28. N. Tancogne-Dejean, M. J. T. Oliveira, X. Andrade, H. Appel, C. H. Borca, G. Le Breton, F. Buchholz, A. Castro, S. Corni, A. A. Correa, U. De Giovannini, A. Delgado, F. G. Eich, J. Flick, G. Gil, A. Gomez, N. Helbig, H. Hübener, R. Jestädt, J. Jornet-Somoza, A. H. Larsen, I. V. Lebedeva, M. Lüders, M. A. L. Marques, S. T. Ohlmann, S. Pipolo, M. Rampp, C. A. Rozzi, D. A. Strubbe, S. A. Sato, C. Schäfer, I. Theophilou, A. Welden, and A. Rubio, "Octopus, a computational framework for exploring light-driven phenomena and quantum dynamics in extended and finite systems," J. Chem. Phys. **152**, 124119 (2020).

29. G. Onida, L. Reining, and A. Rubio, "Electronic excitations: density-functional versus many-body Green's-function approaches," Rev. Mod. Phys. **74**, 601–659 (2002).

30. C. Hartwigsen, S. Goedecker, and J. Hutter, "Relativistic separable dual-space Gaussian pseudopotentials from H to Rn," Phys. Rev. B **58**, 3641–3662 (1998).

31. N. Tancogne-Dejean and A. Rubio, "Atomic-like high-harmonic generation from two-dimensional materials," Science Advances **4**, eaao5207 (2018).

Supplementary Material For:
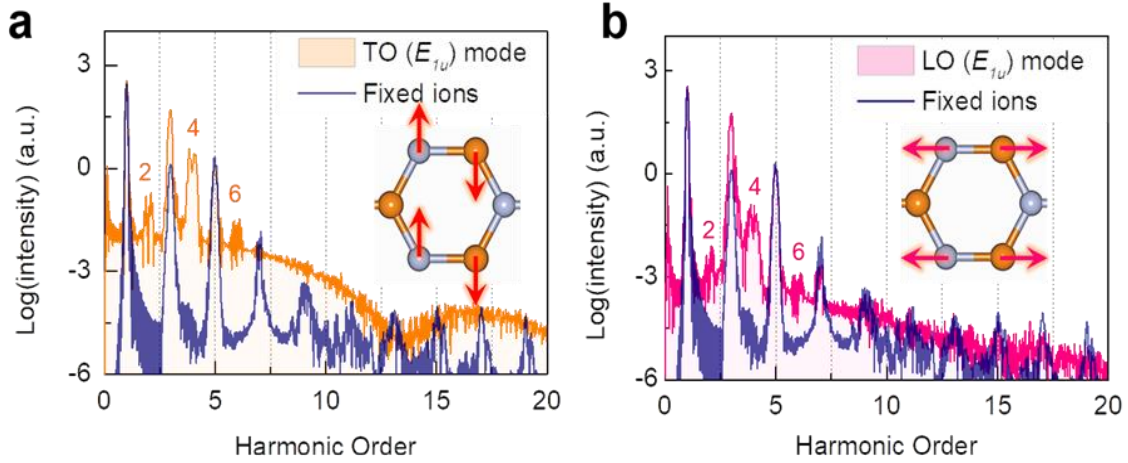# Optically-Induced Symmetry Breaking via Nonlinear Phononics

Figure S1: (a) HHG spectrum for the pump laser parallel with TO (E_{1u}) mode. (b) HHG spectrum for the pump laser parallel with LO (E_{1u}) mode. Here, we employ an in-plane electric field with a wavelength of $\lambda = 800$ nm and an intensity of $I = 10^{12}$ W /cm^2, and a pulse duration of 25-fs full width at half maximum.
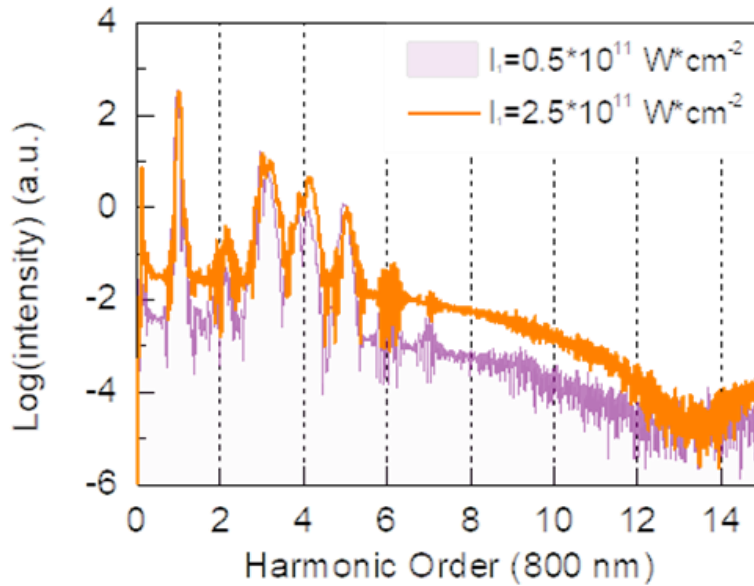

Figure S2: HHG spectra for different pump laser intensities. Here, the polarizations of pump and probe laser are parallel with TO (E_{1u}) mode (pump laser with a wavelength of $\lambda = 7300$ nm). For the probe laser, we use an in-plane driving electric field with a wavelength of $\lambda = 800$ nm and an intensity of $I = 10^{12}$ W/cm^2, and a pulse duration of 25-fs full width at half maximum.